Engineering xxx (xxxx) xxx

Contents lists available at ScienceDirect

Engineering

journal homepage: www.elsevier.com/locate/eng

Research
Environmental Engineering—Article

Highly Selective Singlet Oxygen Generation via an Asymmetric Co–O–Fe Dual-site for Enhanced Water Treatment: Importance of Switching the Ozone Activation Pathway

Qian Hu [a,b], Shanli Wang [a,c], Kaixing Fu [b], Guangpeng Yang [d], Licong Xu [a,c], Wenbin Jiang [a], Minghua Wu [a,c], Wangyang Lu [a], Xiaomin Zhu [a,c], Jinming Luo [b,*]

[a] State Key Laboratory of Bio-based Fiber Materials, Zhejiang Sci-Tech University, Hangzhou 310018, China
[b] State Key Laboratory of Green Papermaking and Resource Recycling, School of Environmental Science and Engineering, Shanghai Jiao Tong University, Shanghai 200240, China
[c] Engineering Research Center for Eco-Dyeing and Finishing of Textiles, Zhejiang Sci-Tech University, Hangzhou 310018, China
[d] Rezel Catalysts Corporation, Shanghai 201313, China

ARTICLE INFO

Article history:
Received 21 February 2025
Revised 12 November 2025
Accepted 18 December 2025
Available online xxxx

Keywords:
Catalytic ozonation
Asymmetric Co–O–Fe dual-site
Activation pathway
Singlet oxygen
Water treatment

ABSTRACT

The singlet oxygen ($^1O_2$)-driven nonradical oxidation pathway has shown great promise for the degradation of organic pollutants with high ionization potentials (IPs) in complex water matrices because of its longer half-life and stronger resistance to environmental interference. However, the symmetric configuration of the active sites (e.g., Fe–O–Fe) in heterogeneous catalysts largely restricts the efficacy of $^1O_2$ generation during ozone activation. In this study, we constructed an asymmetric Co–O–Fe dual-site in bimetallic metal organic frameworks (MOFs) with enhanced electron delocalization to switch the ozone activation pathway from radical-dominant to nonradical-dominant. By combining experimental and theoretical analyses, we revealed that breaking the symmetry of iron sites with Co incorporation optimizes the local electronic structure, thereby facilitating ozone adsorption and reducing the O O bond scission energy barrier to produce $^1O_2$. As a result, the constructed asymmetric Co–O–Fe dual-site demonstrates impressive 6.6 and 2.0 fold increases in $^1O_2$ selectivity and phenol degradation efficiency, surpassing the performance of the state-of-the-art ozonation catalysts. Furthermore, the Co–O–Fe dual-site/O_3 system could efficiently and stably remove diverse high-IP organic pollutants in complex water matrices, following a positive linear correlation (R^2 > 0.97) between the kinetic rate constants and theoretical IP values, which further highlights the unique and critical role of $^1O_2$. This work advances the understanding and design of efficient dual-site catalysts for selective $^1O_2$ generation and sustainable high-IP pollutant degradation.

© 2025 THE AUTHORS. Published by Elsevier LTD on behalf of Chinese Academy of Engineering and Higher Education Press Limited Company. This is an open access article under the CC BY-NC-ND license (http://creativecommons.org/licenses/by-nc-nd/4.0/).

1. Introduction

Ever-increasing worldwide water scarcity is one of the most serious challenges impeding the achievement of sustainable development goals [1,2]. As a promising solution to address this issue, wastewater reclamation has received considerable attention in both academic and industrial fields, in which removing recalcitrant organic pollutants with high ionization potentials (IPs) is an indispensable operation [3]. Heterogeneous catalytic ozonation (HCO) has emerged as a powerful and reliable approach for wastewater decontamination and is governed by the reactive oxygen species (ROS) derived from ozone activation on the catalyst surface [4,5]. In particular, radical and nonradical oxidation pathways, classified by the dominant ROS types, have been demonstrated to elucidate the catalytic paradigm in the HCO process [6]. The radical pathway relies on the generation and utilization of classical hydroxyl radicals (·OH), which have a short lifetime and high sensitivity to coexisting components [7], thereby compromising their practicality for broad applications. In contrast, the latter, with moderate reactive singlet oxygen ($^1O_2$) generation, has been recognized as an alternative method for degrading organic pollutants and presents outstanding stability against environmental interference [8,9]. However, the efficient and sustainable generation of $^1O_2$ is often limited by poor selectivity and an elusive mechanism. Therefore,

* Corresponding author.
E-mail address: jinming.luo@sjtu.edu.cn (J. Luo).

https://doi.org/10.1016/j.eng.2025.12.016
2095-8099/© 2025 THE AUTHORS. Published by Elsevier LTD on behalf of Chinese Academy of Engineering and Higher Education Press Limited Company.
This is an open access article under the CC BY-NC-ND license (http://creativecommons.org/licenses/by-nc-nd/4.0/).

Please cite this article as: Q. Hu, S. Wang, K. Fu et al., Highly Selective Singlet Oxygen Generation via an Asymmetric Co–O–Fe Dual-site for Enhanced Water Treatment: Importance of Switching the Ozone Activation Pathway, Engineering, https://doi.org/10.1016/j.eng.2025.12.016

developing advanced heterogeneous catalysts with rationally designed active sites is highly desirable to achieve precise control over the activation pathway of ozone.

In principle, the activation of ozone at catalytic active sites involves a series of processes, including adsorption, interaction, and evolution [10]. The interaction primarily determines the subsequent evolution of ozone molecules for specific ROS generation, while the adsorption process heavily relies on the porous structure of catalysts to facilitate mass transfer [11,12]. This interaction is dependent mainly on the motifs of the active centers responsible for electron transfer, such as surface hydroxyl groups, Lewis acid sites (LASs), and carbonaceous structural defects [6]. LASs in metal-based catalysts (e.g., metal organic frameworks (MOFs) and metal oxides) have demonstrated great promise in ozone activation and are reported to outperform carbonaceous catalysts (e.g., carbon nanotubes and graphene nanosheets) in terms of both activity and stability [13]. Notably, metal sites tend to form bonds with the terminal oxygen atom of ozone through Lewis acid base interactions. The subsequent elongation and cleavage of the peroxide bond, induced by electron transfer from the metal centers, are crucial for both the activity and selectivity of ozone activation [9]. Moreover, the efficiency of electron transfer can be enhanced by tuning the microenvironments of the metal centers, including the coordination environments and electronic configurations [8,14]. Unfortunately, precisely controlling the microenvironment of metal centers to regulate interactions with ozone and thus steer selective oxidation pathways remains a significant challenge.

Recently, the asymmetric dual-site configuration incorporating heterometal atoms through bridged linkages has been proposed as a means to easily modulate the microenvironment (e.g., electronic structure) of active sites, thereby presenting significant opportunities for enhancing catalytic activity [15,16]. The electronic distribution of metal centers is substantially affected by interactions within dual-sites due to the diverse chemical environments involved [17,18]. This interaction allows for improved polarization of the active sites for terminal oxygen bonding and subsequent electron transfer, which in turn increases the selective generation of ROS [19,20]. For example, Cu–O_v–In sites in Cu-doped In_2O_3 have accelerated electron transfer to the O–O bond in PMS for radical generation, resulting in an increase of nearly 31.8 times over that of symmetric sites in terms of pollutant degradation [18]. Conversely, the contiguous Mn–N and Co–N sites with tight electronic coupling between Mn and Co have exhibited considerable potential for promoting $^1O_2$ generation from PMS activation [21]. Despite the above progress in the elucidation of asymmetry, the functionality of dual-sites in steering ozone activation pathways remains elusive. It is also unclear whether the designed metal centers incorporated with bridged heterometal atoms can facilitate a nonradical pathway dominated by $^1O_2$. Thus, the catalytic ozonation performance and mechanism of heterometal bridging active dual-sites deserve in-depth investigation.

Since MOFs are atomically constructed from the programmable self-assembly of metal oxo clusters and organic linkers [22,23], the precise regulation of asymmetric bimetallic centers with tailored configurations in MOFs is more feasible and available than that of conventional catalysts, such as metal oxides and single atoms [24,25]. In this study, we employed MIL-53(Fe), a typical iron-based MOF identified by an ·OH-dominated HCO process in our previous works [11,26,27], as a model catalyst to validate the possibility of a catalysis pathway switch enabled by the construction of heterometal-oxo nodes. We synthesized O-bridged Co–O–Fe dual-sites instead of Fe–O–Fe nodes within MIL-53(Fe) through doping engineering to approach novel asymmetric dual-sites containing Co and Fe atoms. Following a systematic evaluation of ROS formation and pollutant degradation performance, we observed a significant improvement in the selective generation of $^1O_2$ due to changes in the symmetry of the iron sites. This leads to potent catalytic ozonation activity and stability for the degradation of organic pollutants with high IPs. Through density functional theory (DFT) calculations and experimental analysis, we further explored how the ozone activation pathway switched into a nonradical regime. The critical role of the cobalt atom in optimizing the electronic structure of the asymmetric iron centers for selective $^1O_2$ generation was also discussed. Our work provides fundamental advancements toward the rational design of effective catalysts for realizing a $^1O_2$-dominated catalytic ozonation process at the atomic level.

2. Materials and method

2.1. Chemicals and reagents

Iron chloride hexahydrate ($FeCl_3·6H_2O$), cobalt chloride hexahydrate ($CoCl_2·6H_2O$), p-phthalic acid (H_2BDC, $C_8H_6O_4$), 4-amino-2,2,6,6-tetramethylpiperidine (TEMP, $C_9H_{20}N_2$), 5,5-dimethyl-1-pyrroline *N*-oxide (DMPO, $C_6H_{11}NO$), p-benzoquinone (p-BQ, $C_6H_4O_2$), furfuryl alcohol (FFA, $C_5H_6O_2$), humic acid (HA, ≥90%), coumarin ($C_9H_6O_2$), metronidazole (MDE, $C_6H_9N_3O_3$), 4-aminophenol (4-AP, C_6H_7NO), hydroquinone (HQ, $C_6H_6O_2$), phenol (C_6H_6O), p-chlorophenol (4-CP, C_6H_5ClO), p-nitrophenol (4-NP, $C_6H_5NO_3$), and 4-nitrochlorobenzene (4-NC, $C_6H_4ClNO_2$) were purchased from Aladdin Chemical Co., Ltd., China. Ethanol (C_2H_6O), methyl alcohol (MeOH, CH_3OH), *N*,*N*-dimethylformamide (DMF, C_3H_7NO), tetrachloromethane (CCl_4), chlorhydric acid (HCl, 37.5 wt%), sodium hydroxide (NaOH), sodium thiosulfate ($Na_2S_2O_3$), sodium sulfate (Na_2SO_4), sodium carbonate (Na_2CO_3), sodium bicarbonate ($NaHCO_3$), and sodium chloride (NaCl) were obtained from Hangzhou Gaojing Chemical Co., Ltd, China. Tert-butyl alcohol (TBA, $C_4H_{10}O$) were provided by Shanghai Macklin Biochemical Co., Ltd, China. Ultrapure water, produced from Milli-Q Advantage A10 (Millipore) system, was utilized in all experiments.

2.2. Preparation of bimetallic and monometallic MOFs

Bimetallic metal organic framework (denoted as MIL-53(FeCo)) was synthesized via a facile doping engineering incorporated with the typical solvothermal method. Typically, 4 mmol of $CoCl_2·6H_2O$ and 16 mmol of $FeCl_3·6H_2O$ were simultaneously added into 120 ml of DMF to obtain the precursor solution, in which the ration of Co and Fe atom was maintained at 1:4. Subsequently, 20 mmol of H_2BDC was dissolved into the precursor solution under moderate stirring. The obtained solution in a Teflon autoclave was subjected to a crystallization process at 150 °C for 18 h. The crystallization time was chosen because we have revealed the regulation mechanism to yield effective MIL-53(Fe) catalyst for a radical pathway in our previous work [11]. After cooling to room temperature, the product was centrifuged and washed by DMF and ethanol for several times prior to drying in a vacuum oven at 100 °C for overnight. The synthesis of monometallic MIL-53(Fe) was conducted by the same procedure for bimetallic MIL-53(FeCo), except only using 20 mmol of $FeCl_3·6H_2O$ without $CoCl_2·6H_2O$ addition.

The details of the catalyst characterization, HCO experiments, analytical methods, and theoretical calculations are described in the Supporting Information (Texts S1–S4 in Appendix A).

3. Results and discussion

3.1. Characterizations of bimetallic MOFs with asymmetric Co–O–Fe dual-site configurations

The asymmetric Co–O–Fe dual-site configurations within bimetallic MIL-53(FeCo) were constructed via a straightforward

doping strategy (Fig. 1(a)), where $CoCl_2·6H_2O$ was introduced to partially replace the iron centers. Owing to the similar bond energies at 298 K of Co–O ((397.4 ± 8.7) kJ·mol^{-1}) and Fe–O ((407.00 ± 1.0) kJ·mol^{-1}) [28], the Co–O–Fe dual-site configuration is expected to form competitively as the crystallization temperature increases. This dual-site configuration is anticipated to be well anchored within the porous framework of MIL-53(FeCo), ensuring easy accessibility. Since metal–oxo nodes are critical for regulating the physicochemical properties of MOFs and achieving their catalytic functions, elucidating the microenvironmental changes in iron centers upon cobalt doping is essential. The porous structure of the catalysts was characterized by N_2 adsorption desorption measurements. As shown in Fig. S1(a) in Appendix A, both bimetallic MIL-53(FeCo) and monometallic MIL-53(Fe) exhibited classical type-IV isotherms with H3 hysteresis loops, indicative of a mesoporous structure. The pore size distribution (Fig. S1(b)) was primarily in the range of 2–10 nm, with the bimetallic MIL-53 (FeCo) displaying a higher intensity, suggesting a greater abundance of mesopores. According to the Brunauer Emmett–Teller (BET) analysis, the specific surface area (SSA) of MIL-53(FeCo) was significantly greater than that of MIL-53(Fe) (Table S2 in Appendix A). Moreover, cobalt doping led to a substantial increase in the total pore volume, from 0.004 to 0.068 cm^3·g^{-1}.

The powder X-ray diffraction (PXRD) patterns (Fig. 1(b)) of bimetallic MIL-53(FeCo) and monometallic MIL-53(Fe) exhibit identical characteristic peaks at 9.4°, 12.6°, 18.9°, 22.1°, and ~25.9°, corresponding to the (220), (120), (121), (031), and (240) facets, respectively. The positioning of these peaks aligns well with

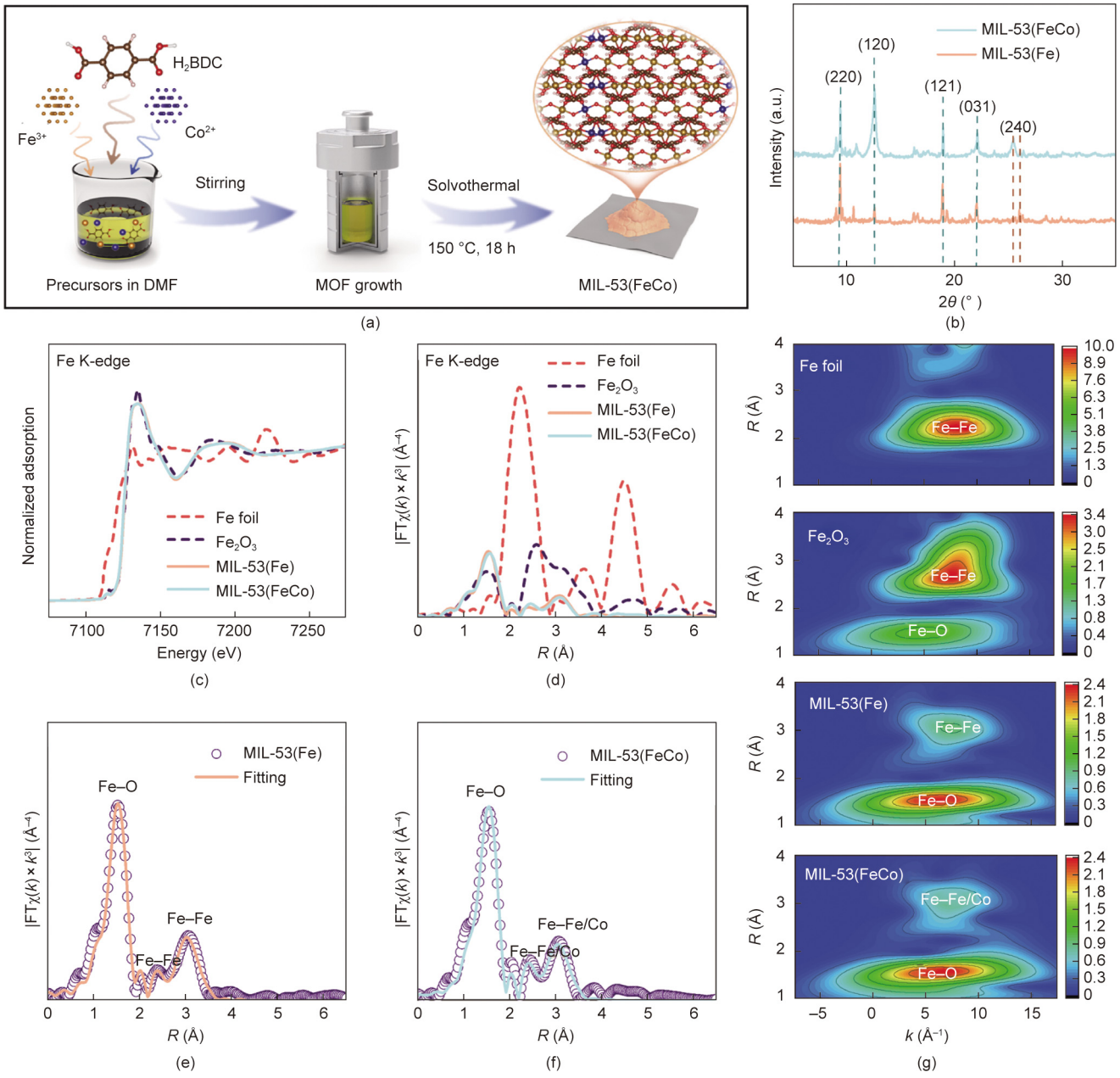

Fig. 1. Characterizations and atomic structures of monometallic MIL-53(Fe) and bimetallic MIL-53(FeCo). (a) Schematic diagram of the preparation process of bimetallic MIL-53(FeCo). (b) PXRD patterns of monometallic MIL-53(Fe) and bimetallic MIL-53(FeCo). (c) Fe K-edge XANES spectra and (d) FT k^3-weighted Fe K-edge EXANES spectra of monometallic MIL-53(Fe) and bimetallic MIL-53(FeCo). FT-EXAFS fitting curves for (e) monometallic MIL-53(Fe) and (f) bimetallic MIL-53(FeCo). (g) WT-EXAFS spectra of Fe foil, Fe_2O_3, MIL-53(Fe), and MIL-53(FeCo).

previous reports [29,30], confirming the successful synthesis of MIL-53-type MOFs. However, we observed that the peak at 25.9° slightly shifted toward a lower angle (25.4°), which can be attributed to the fact that the ionic radius of Co^{2+} (0.074 nm) is much greater than that of Fe^{3+} (0.064 nm) [31,32]. Additionally, the intensity ratio between the peaks at 12.6° and 9.4° significantly increased from 0.27 to 1.34 (Table S3 in Appendix A), which intriguingly parallels our earlier findings regarding the timescale-dependent crystal evolution process [11]. This suggests that the introduction of the heterometallic Co accelerated the crystal evolution of MIL-53(Fe), resulting in a similar effect on the crystal structure modulation as that of extending the solvothermal time. As illustrated in Fig. S2 in Appendix A, we observed a bipyramidal hexagonal prism morphology for monometallic MIL-53(Fe), which features numerous distinct cracks. In contrast, the bimetallic MIL-53(FeCo) manifested an irregular fragment shape, likely resulting from the collapse of the original particles. This morphological evolution aligns with the principles of timescale-dependent crystal growth observed in the PXRD analysis. Given that the bond dissociation energy at 298 K of Co–O ((397.4 ± 8.7) $kJ \cdot mol^{-1}$) is slightly lower than that of Fe–O ((407.00 ± 1.0) $kJ \cdot mol^{-1}$) [28], it is plausible that the collapse of bimetallic MIL-53(FeCo) particles occurs more readily, as some Fe–O–Fe nodes are replaced with Co–O–Fe configurations. As shown in Figs. S3 and S4 in Appendix A, the coexistence of color-marked dots indicates a uniform distribution of C, O, Fe, and Co within the bimetallic MIL-53(FeCo). These results strongly suggest the successful construction of Co–O–Fe dual-sites by doping engineering.

To further investigate the formation of the Co–O–Fe dual-site configuration, we employed Fourier transform infrared (FT–IR), Raman, and X-ray photoelectron spectroscopy (XPS) to gain comprehensive insights into the chemical structures of the bimetallic MIL-53(FeCo) and monometallic MIL-53(Fe) catalysts. As shown in Fig. S5(a) in Appendix A, the fingerprint of C–H bonding vibrations and carboxyl group vibrations in the organic linkers is clearly observed in the FT–IR spectra [33]. The broad band located at 3429 cm^{-1} is associated with O–H stretching vibrations of water molecules adsorbed or bound to the catalyst surface [34]. Notably, the absorption peak at a lower wavenumber of approximately 550 cm^{-1} is attributed to the stretching vibration of the metal oxygen bond mode. In the case of monometallic MIL-53(Fe), the signal observed at 552 cm^{-1} is attributed to Fe–O–Fe stretching vibrations, whereas in bimetallic MIL-53(FeCo), the corresponding peak redshifts to 544 cm^{-1} (Fig. S5(b) in Appendix A), suggesting the formation of Co–O–Fe configurations [34]. Similarly, we detected a new band at 1497 cm^{-1} in the Raman spectrum of bimetallic MIL-53(FeCo) (Fig. S6(a)) and a slightly lower shift in the characteristic peak (455 cm^{-1}) for the metal-oxo (Fig. S6(b)), confirming the successful formation of the Co–O–Fe dual-site configuration together with the results of the XRD analysis [35–39]. The XPS spectra presented in Figs. S7–S10 in Appendix A indicate that both MIL-53(Fe) and MIL-53(FeCo) mainly consist of C, O, and Fe. The emergence of a new peak at 785.1 eV in the spectra of bimetallic MIL-53(FeCo) (Fig. S7) and the observation of two peaks at 783.8 and 797.3 eV in the high-resolution Co 2p XPS spectrum (Fig. S9 (b)) confirm the presence of Co [40], suggesting successful cobalt incorporation into MIL-53(Fe). Notably, the bimetallic MIL-53 (FeCo) displays a slightly lower binding energy (711.5 eV) for Fe $2p_{3/2}$ compared to that of MIL-53(Fe) (711.7 eV; Fig. S9(a)). This observation indicates that the integration of cobalt increases the electron density around the surrounding iron centers, which are bridged by oxygen atoms, due to the induced asymmetry [41]. After cobalt doping, the molar ratio of O_{ads} to O_{latt} slightly decreased from 5.56 to 4.55 (Fig. S10), suggesting the presence of uncoordinated metal sites in the form of metal OH adducts (e.g., Fe OH) [42].

To further confirm the successful construction of the asymmetric Co–O–Fe dual-site configuration, we elucidated the atomic structure and coordination environment of the iron sites in both bimetallic MIL-53(FeCo) and monometallic MIL-53(Fe) through X-ray absorption fine-structure (XAFS) measurements (Figs. 1(c)–(g) and Fig. S11 in Appendix A). The Fe K-edge position in the X-ray absorption near-edge structure (XANES) indicates that the oxidation state of Fe in both catalysts is very close to that of standard Fe_2O_3, which is +3 (Fig. 1(c)). Compared with the symmetric Fe–O–Fe configuration, the asymmetric Co–O–Fe dual-site results in a slightly lower adsorption edge position for Fe, suggesting a decreased valence state [43], which is consistent with the XPS results (Fig. S9(a)). Compared with the symmetric Fe O Fe configuration, the observed decrease in the intensity of the pre-edge peak and increase in the intensity of the white-line peak in the Co–O–Fe dual-site confirm the increased asymmetry and rearranged charge polarization, thereby optimizing the coordination environment of the Fe atoms upon Co doping (Fig. 1(c)) [20,44]. This alteration may impact the local electron density of iron sites, thereby influencing their catalytic activity and/or selectivity [45]. The Fourier transform (FT) curves derived from the extended X-ray absorption near-edge structure (EXAFS) spectra at the Fe K-edge are shown in Fig. 1(d), with the corresponding fitting results summarized in Figs. 1(e)–(f) and S11 and Table S4 in Appendix A. Notably, the dominant peak in the R-space for bimetallic MIL-53(FeCo) is located at 1.57 Å, whereas for monometallic MIL-53(Fe), it is located at 1.53 Å, corresponding to the first shell layer of Fe O coordination [46]. The lack of a characteristic Fe Fe signal at 2.21 Å indicates that no Fe Fe bond formation occurred, indicating a well-dispersed arrangement of atomic iron sites within the prepared catalysts. The small peak observed at 3.08 Å may indicate the presence of the second shell Co–O–Fe dual-site configuration in bimetallic MIL-53(FeCo), which is further corroborated by wavelet-transformed (WT) EXAFS analysis (Fig. 1(g)). Notably, a slight contraction in the maximum peak at k = 7.60 $Å^{-1}$ is observed for bimetallic MIL-53(FeCo) compared with MIL-53(Fe), highlighting the formation of oxygen-bridged asymmetric Co–O–Fe dual-sites. Additionally, the EXAFS fitting analysis indicates that the first shell coordination numbers of the central iron atom are 4.3 for MIL-53(Fe) and 4.7 for MIL-53(FeCo), respectively, suggesting that fewer defective iron sites are generated upon Co doping (Table S4), which is further supported by solid electron paramagnetic resonance (EPR) measurements (Fig. S12 in Appendix A). In this context, the construction of the asymmetric Co–O–Fe dual-site configuration has been systematically validated in a bimetallic MIL-53(FeCo) catalyst.

3.2. Identification of ozone activation pathways in symmetric and asymmetric configurations

Radical and nonradical pathways are frequently involved in HCO processes, and these pathways are influenced by the microenvironment at the active sites [10]. To elucidate the specific dominant pathway, we investigated the generation and contributions of $^1O_2$ and ·OH species. For both monometallic and bimetallic MIL-53 (FeCo) catalysts initiating HCO processes, the formation of ROS was first identified via solution EPR spectroscopy. The EPR spectra (Fig. 2(a)) revealed that when DMPO was used as an effective trapping agent in water, a characteristic 1:2:2:1 quadruple peak pattern corresponding to the DMPO-·OH adduct [47] was observed during catalytic ozonation involving monometallic MIL-53(Fe). In contrast, no significant EPR signals were detected in the absence of the catalyst (ozonation alone) or in the bimetallic MIL-53(FeCo)/O_3 system. These findings indicate that the Fe–O–Fe configuration present in monometallic MOFs preferentially catalyzes the decomposition of ozone into ·OH, thereby favoring a radical pathway. Conversely, the

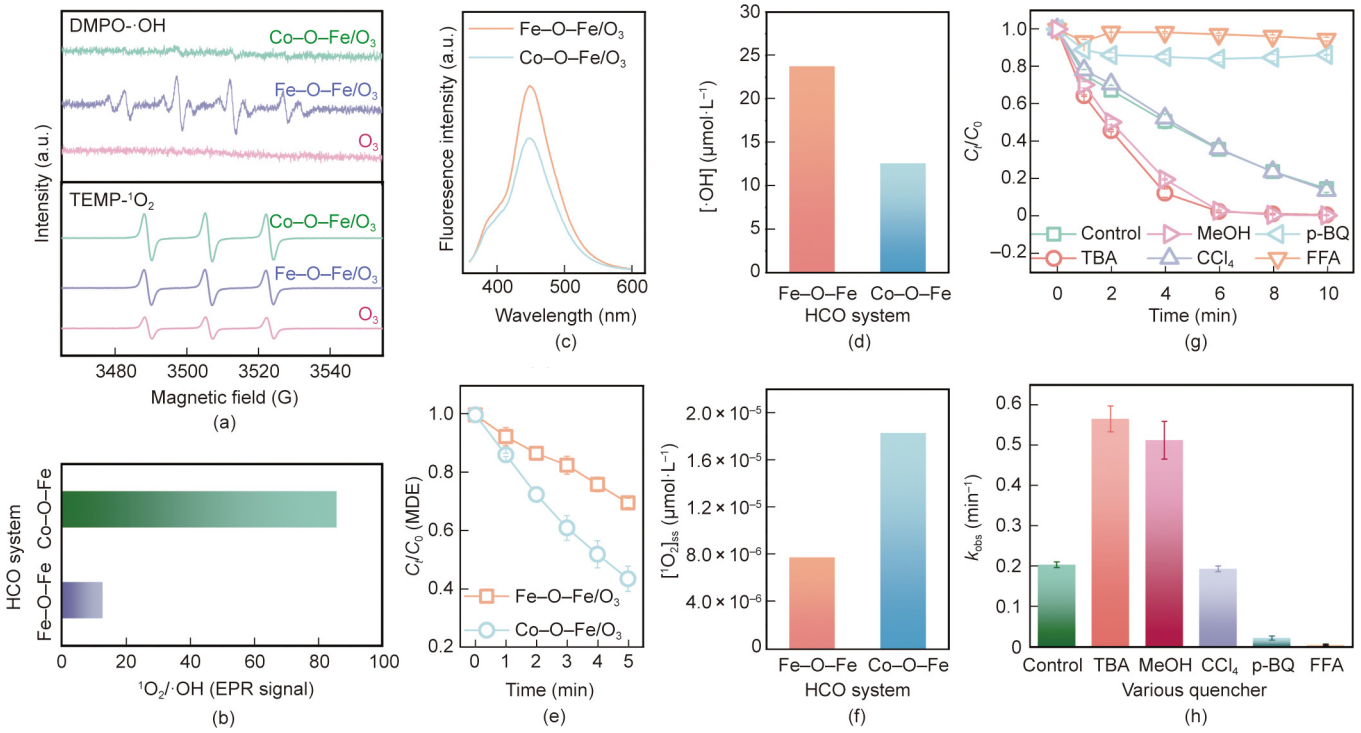

Fig. 2. Performance of the asymmetric Co–O–Fe dual-site for selective $^1O_2$ production from ozone activation. (a) EPR tests for different systems using DMPO and TEMP as trapping agents. (b) $^1O_2$ selectivity of the Fe–O–Fe and Co–O–Fe configurations. (c) Fluorescence emission peak of 7-HOC, (d) [·OH], (e) degradation rate of the MDE probe, and (f) $[^1O_2]_{ss}$ in the Fe–O–Fe and Co–O–Fe configurations initiated HCO systems. C_0 and C_t represent the contaminants concentration at the initial state and at time t, respectively. (g) Effects of various scavengers on the degradation of 4-NP in Co–O–Fe configuration initiated by the HCO system and (h) the corresponding k_{obs} values. Reaction conditions: ozone input dosage = 0.42 mmol·L^{-1}·min^{-1}, catalysts = 0.1 g·L^{-1}, $C_{coumarin,\ 0}$ = 10 mmol·L^{-1}, $C_{MDE,\ 0}$ = 20 mg·L^{-1}, $C_{4\text{-}NP,\ 0}$ = 50 mg·L^{-1}, $C_{TBA,\ 0}$ = $C_{MeOH,\ 0}$ = $C_{CCl4,\ 0}$ = $C_{p\text{-}BQ,\ 0}$ = $C_{FFA,\ 0}$ = 2 g·L^{-1}, temperature (T) = 25 °C. C: concentration.

Co–O–Fe configuration in the bimetallic MIL-53(FeCo) system effectively suppresses the radical pathway by limiting the generation of ·OH. This indicates the ability of the bimetallic configuration to switch product formation away from radicals, instead of promoting alternative reaction pathways, thus enhancing the overall efficiency of ozone decomposition.

Building on this intriguing observation, we further investigated the role of the nonradical pathway by employing TEMP as the trapping agent, with water serving as the solvent for the EPR spectra recordings. Our analysis revealed the presence of a threefold peak with a signal intensity ratio of 1:1:1 in all the tested systems, which we attributed to the TEMP-$^1O_2$ adduct [48]. Notably, the strongest signal for $^1O_2$ was clearly observed in the bimetallic MIL-53(FeCo)/O_3 system compared with the other two counterparts. This finding indicates highly efficient and selective generation of $^1O_2$ via a nonradical pathway facilitated by Co–O–Fe dual-sites. Semiquantitative analysis indicated that the peak intensity for the bimetallic MIL-53(FeCo)/O_3 system was 2.22 times greater than that of the ozonation alone system and 1.36 times greater than that of the monometallic MIL-53(Fe)/O_3 system, with the signal from ozonation alone defined as unity. Additionally, superoxide radicals ($\cdot O_2^-$), a key intermediate in the generation of both $^1O_2$ and ·OH during HCO chain reactions [10], were detected in the Fe-MOF-based systems (Fig. S13 in Appendix A). Notably, the bimetallic MIL-53(FeCo)/O_3 system presented a relatively lower $\cdot O_2^-$ signal intensity, likely reflecting its greater contribution to $^1O_2$ generation [49]. Interestingly, we were unable to detect $\cdot O_2^-$ signals in the ozonation-only system, highlighting the effective catalytic nature of the designed iron-based MOFs. By utilizing the intensity ratio of the $^1O_2$ and ·OH signals as a simplified descriptor for selectivity (Fig. 2(b)), we found that the selectivity for the nonradical pathway could be enhanced by 6.6 times in the case of the Co–O–Fe configurations. These results clarify that modifying the iron sites from Fe–O–Fe configurations to asymmetric Co–O–Fe dual-sites through doping engineering can effectively switch the ozone activation pathway from radical to nonradical. This transition significantly regulates the preference for generating $^1O_2$ over ·OH in the HCO process.

To investigate the capacity for switching pathways, we evaluated the accumulated concentration of ·OH, denoted as [·OH], generated during ozonation alone and in the HCO process via a fluorescence method with coumarin as the probe. The coumarin molecule is readily oxidized to form 7-hydroxylcoumarin (7-HOC), achieving a selectivity of 29% [50]. As illustrated in Fig. 2(c), a distinct fluorescence emission peak at 450 nm corresponding to 7-HOC was observed in the fluorescence spectra after a reaction time of 30 minutes. However, in the ozonation-only system, a significant overlapping doublet obscured the peak at 450 nm. Taking into account the EPR observations (Fig. 2(a)), we utilized the overlapping doublet spectrum as a background to correct for its contribution. In contrast, both the bimetallic and monometallic catalysts in the HCO processes presented increased fluorescence intensity, indicative of increased ·OH generation, which aligned well with the EPR results. Furthermore, the difference in fluorescence intensity between the two catalysts highlighted their divergent capacities for selectively decomposing ozone into ·OH. The corresponding [·OH] were determined to be 12.6 μmol·L^{-1} for the bimetallic MIL-53(FeCo) catalyst and 23.8 μmol·L^{-1} for the monometallic MIL-53(Fe) catalyst (Fig. 2(d)). This result indicates that the bimetallic MIL-53(FeCo) catalyst effectively hinders the radical pathway, reducing ·OH generation by a factor of 1.9 compared with that of the monometallic MIL-53(Fe). The fluorescence spectra and [·OH] as a function of reaction time are presented in Figs. S14 and S15 in Appendix A, respectively. In terms of the dynamic generation of ·OH, the bimetallic MIL-53(FeCo) catalyst exhibited a kinetic rate constant of 1.09 min^{-1}, which was 37.7% lower than that of the monometallic MIL-53(Fe)

catalyst (1.75 min^{-1}). This reduction in the rate constant can be attributed to the construction of the asymmetric Co–O–Fe dual-sites, which influences the reaction pathway.

We further explored the nonradical pathway by monitoring the steady state concentration of $^1O_2$ ($[^1O_2]_{ss}$) during the HCO process. For this purpose, MDE was used as a specific probe because of its selective reaction with $^1O_2$ in the absence of ·OH. Consequently, the liquid phase was composed of 50% MeOH and 50% water to eliminate any generated ·OH. This selectivity is crucial, given that the second-order rate constants of the MDE for reactions with $\cdot O_2^-$ or ozone are significantly lower (Table S5 in Appendix A) [5]. The calculation details for the $[^1O_2]_{ss}$ are provided in Text S3. As illustrated in Fig. 2(e), the degradation of MDE by the bimetallic MIL-53(FeCo) catalyst was noticeably more effective than that achieved with the monometallic MIL-53(Fe) catalyst, providing evidence for the selective generation of a greater concentration of $^1O_2$. Additionally, the $[^1O_2]_{ss}$ for the bimetallic MIL-53(FeCo) was calculated to be 1.83×10^{-5} μmol·L^{-1}, which is 2.4 times higher than that observed with the monometallic MIL-53(Fe) catalyst (7.78×10^{-6} μmol·L^{-1}) (Fig. 2(f)). The consistency of these results concerning the quantification of the [·OH] and the $[^1O_2]_{ss}$ reinforces our earlier EPR findings. This further confirms the significant effect of iron microenvironment regulation on switching the pathway for ozone activation, highlighting the potential of the bimetallic configuration in enhancing nonradical processes.

The contributions of $^1O_2$ and ·OH species to the degradation of 4-NP, a model substrate with high IP, were assessed through quenching tests. MeOH and TBA were employed as quenchers for ·OH, with MeOH capable of capturing both surface-bound and bulk ·OH, whereas TBA is effective only for bulk ·OH [51]. Interestingly, the results shown in Figs. 2(g) and (h) and Fig. S16 in Appendix A demonstrated that the addition of 2.0 g·L^{-1} TBA or MeOH did not inhibit the removal of 4-NP by the bimetallic MIL-53(FeCo) catalyst, confirming the limited contribution of ·OH to this reaction. Contrary to common expectations, we observed a slight increase in the removal of 4-NP, likely due to the formation of fine bubbles that promote mass transfer [13]. p-BQ is frequently used as a quencher for $\cdot O_2^-$. However, recent studies have indicated that p-BQ may not selectively capture $\cdot O_2^-$ due to its rapid reactions with other oxidizing species [52], such as O_3 and $^1O_2$ (Table S5). Therefore, the significant inhibition observed in Fig. 2(g), caused by p-BQ, could result from the combined quenching of O_3, $^1O_2$, and $\cdot O_2^-$. To specifically assess the role of $\cdot O_2^-$, CCl_4, a selective probe for $\cdot O_2^-$, was utilized in quenching tests [53]. The negligible inhibitory effect on the degradation of 4-NP upon the addition of CCl_4 (Fig. 2(g)) further indicated that $\cdot O_2^-$ plays a minimal role in 4-NP degradation. We subsequently utilized FFA, a well-known scavenger of $^1O_2$, to elucidate the contribution of $^1O_2$ to this process [5]. The presence of FFA resulted in substantial inhibition of 4-NP removal, demonstrating that $^1O_2$ was the predominant ROS in the MIL-53(FeCo)/O_3 system. Specifically, the removal rate of 4-NP significantly decreased by 79.8% in the presence of FFA, with the observed pseudo-first-order kinetic rate constant rate constant (k_{obs}) decreasing 20-fold (Figs. 2(g) and (h) and Fig. S16). In summary, both the EPR measurements and quenching results indicate that the nonradical pathway, rather than the radical pathway, predominates in the bimetallic MIL-53(FeCo)-based HCO process. This difference is likely attributed to the alteration in the configuration of the iron centers within the catalyst.

3.3. Mechanistic insights into the nonradical pathway triggered by asymmetric Co–O–Fe dual-sites

To elucidate the electron distribution in the asymmetric Co–O–Fe dual-site configuration, DFT calculations were performed using two optimized model structures representing bimetallic MIL-53 (FeCo) and monometallic MIL-53(Fe) (Fig. S17 in Appendix A). Bader charge analysis, depicted in Fig. 3(a) and (b), revealed that the losses and gains of electrons from the surface iron and oxygen atoms in monometallic MIL-53(Fe) are −1.60 e and 0.97 e, respectively. This indicates the robust symmetric nature of the Fe–O–Fe motifs, which may limit the catalytic performance of the iron sites [19]. In contrast, in the bimetallic MIL-53(FeCo), the presence of Co rearranges the electron distribution, increasing the electron density of the neighboring iron atom to approximately 0.04 e. This change aligns with the valence shift confirmed by XPS and XFAS measurements. Furthermore, the disparity in Bader charges between Co and Fe, which are bridged by the oxygen atom, highlights the alteration of the surface symmetric site configuration. The constructed asymmetric Co–O–Fe dual-site configuration, characterized by uneven electron distribution and improved strong LASs density (Figs. S18 and S19 and Table S6 in Appendix A) [26], is anticipated to enhance the adsorption and dissociation of reactants and intermediates [54], thereby contributing to altered ozone activation pathways.

Building on this assumption, we conducted additional calculations to explore the differential interactions between ozone molecules and symmetric versus asymmetric configurations [55]. As illustrated in Figs. 3(c) and (d), the electron transfer from the iron sites to the ozone molecule was measured at 0.44 e on the Co–O–Fe dual-sites, significantly surpassing the value of 0.37 e observed for the symmetric Fe–O–Fe configurations. This increased charge transfer enables a more pronounced electronic reconfiguration between the asymmetric Co–O–Fe dual-site and the ozone molecule [19]. Consequently, this reconfiguration elongates the O–O bond in the ozone molecule adsorbed at the iron sites from 1.42 Å in the symmetric Fe–O–Fe system to 1.46 Å in the asymmetric Co–O–Fe dual-sites (Fig. S20 in Appendix A). The extended O–O bond facilitates the subsequent generation of a site-*O/*OO complex with enhanced oxidizing potential [56]. The adsorption energies (E_{ads}) for the systems with asymmetric Co–O–Fe dual-site and symmetric Fe–O–Fe configurations were calculated to be −2.24 and −1.46 eV, respectively (Fig. S20 and Table S7 in Appendix A). The notably lower E_{ads} value for the asymmetric Co–O–Fe dual-sites indicates a much stronger interaction with the ozone molecules than with the Fe–O–Fe configurations. This variation in E_{ads} underscores the critical role of the preferential interaction between asymmetric iron sites and ozone molecules in facilitating catalytic ozonation through oriented nonradical pathways [9,57].

The limiting reaction barrier, which depends on the free energy of the rate-limiting step, is a critical factor influencing catalytic ozonation performance [58]. Fig. 3(e) presents the nonradical activation pathway in catalysis with distinct Co–O–Fe dual-site configurations. This pathway can be simplified into three main steps: (i) ozone molecules adsorb onto the iron sites, forming adsorbed ozone (*O_3(ad)); (ii) generation of a transition state (TS) in the form of an Fe–O_3 complex; and (iii) decomposition of the adsorbed ozone into atomic oxygen (*O) and molecular oxygen (O_2) species. The iron site is then regenerated through the reaction of the generated *O with another ozone molecule, as referenced in previous reports [58]. Compared with the iron sites in the symmetric Fe–O–Fe configurations, the asymmetric Co–O–Fe dual-site results in a significantly lower energy state for ozone activation (Fig. 3(f)). Notably, the ozone adsorption energy for the asymmetric Co–O–Fe dual site is considerably more negative (−2.24 eV) than that of the symmetric Fe–O–Fe configuration (−1.46 eV). This suggests that introducing cobalt to induce asymmetry is an effective strategy to increase the adsorption strength at the active sites. Consequently, the energy barrier of the reaction intermediates can be optimized, facilitating the production of *O and O_2 species through the elongation and dissociation of the O O bond. This aligns with experimental findings indicating that the asymmetric Co–O–Fe

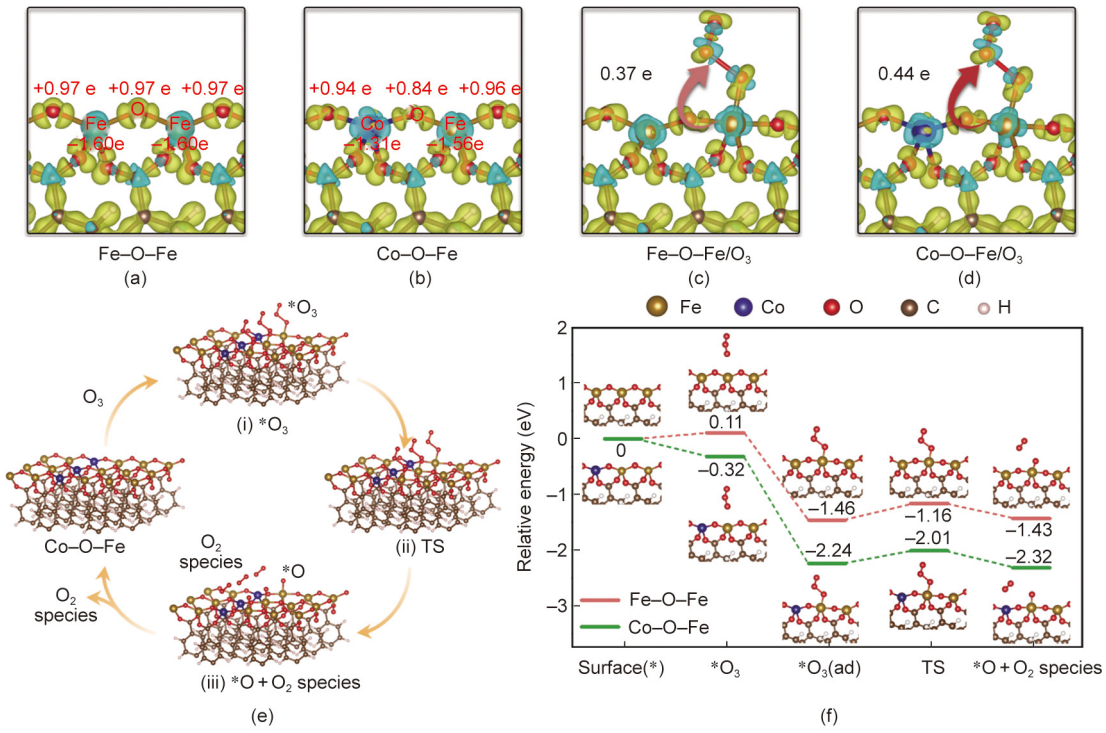

Fig. 3. Theoretical activity and selectivity of asymmetric Co–O–Fe dual-sites. Bader charge of the (a) Fe–O–Fe and (b) Co–O–Fe configurations. Electron transfer from the iron sites on the (c) Fe–O–Fe and (d) Co–O–Fe configurations to the ozone molecule. The yellow and cyan regions represent electron accumulation and electron depletion, respectively. (e) Proposed nonradical pathway for catalytic ozonation via the Co–O–Fe dual-site configuration. (f) Relative energy diagram for the nonradical ozone activation pathway in catalysis with the Fe–O–Fe and Co–O–Fe configurations.

dual site is more efficient in ozone activation and the generation of $^1O_2$. To elucidate the formed O_2 species, we further calculated its spin population via DFT. As shown in Fig. S21 in Appendix A, the spin population of the O_2 species generated on the asymmetric Co–O–Fe dual-site is 0.02, in contrast to the 1.62 observed for the Fe–O–Fe configuration. This result indicates the preferential generation of $^1O_2$ in the asymmetric structure [59]. Therefore, the differences in interactions between the symmetric and asymmetric iron sites and the ozone molecule lead to varied dissociation barriers for the Fe–$^*O_3$ complexes. This ultimately contributes to the asymmetry-dependent efficiency of ozone activation and selectivity for $^1O_2$ generation.

3.4. Catalytic performance for degradation of organic pollutants with high Ips

The catalytic ozonation performances of the Co–O–Fe and Fe–O–Fe configurations were investigated for their ability to degrade organic pollutants, with phenol used as a representative high-IP [3,60]. In the absence of ozone, both the bimetallic and monometallic MIL-53(Fe) could remove only 3.0% of phenol (Fig. S22 in Appendix A) through adsorption effects attributed to their mesoporous structures (Fig. S1 and Table S2), which help concentrate reactants and substrates around the active sites for enhanced degradation [61]. For the catalytic ozonation system utilizing monometallic MIL-53(Fe) (i.e., the symmetric Fe–O–Fe configuration), phenol degradation approached completion, with an k_{obs} of 0.27 min^{-1}. In comparison, the degradation rate of phenol with the asymmetric Co–O–Fe dual-site reached 100% removal with more than a two-fold increase in k_{obs} (0.55 min^{-1}), indicating significantly superior degradation performance due to the incorporation of heterometallic Co. Given that $^1O_2$ preferentially attacks electron-rich organic compounds while ·OH undergoes nonselective oxidation, we further evaluated the degradation of 4-NP, which is characterized by its higher electron deficiency, to elucidate the role of asymmetry in selective ozone activation. As shown in Fig. S23 in Appendix A, the bimetallic MIL-53(FeCo) displayed a slight decrease in both the degradation rate and k_{obs} for 4-NP removal compared with those of the monometallic MIL-53(Fe). The MIL-53(FeCo)-initiated HCO process achieved an 85.2% removal efficiency of 4-NP with a k_{obs} of 0.20 min^{-1}, which is lower than the k_{obs} of the MIL-53(Fe) system (0.27 min^{-1}). Interestingly, we observed identical k_{obs} values for both phenol and 4-NP degradation when MIL-53(Fe) was used as the catalyst; however, MIL-53 (FeCo) exhibited an inferior decomposition capacity for 4-NP compared with phenol (Fig. S24 in Appendix A). The disparity in degradation capacity between the MIL-53(FeCo) and MIL-53(Fe) catalysts toward electron-rich phenol and electron-deficient 4-NP may result from the differing oxidation potentials of the main ROS generated from ozone decomposition [4,9]. These results collectively suggest that the ozone activation pathway has shifted from a radical-dominant mechanism to a nonradical-dominant mechanism, further supporting the prevailing generation and contribution of $^1O_2$ as governed by the asymmetry of the active sites. Moreover, the enhanced electron transfer capacity of MIL-53(FeCo) (Fig. S25 in Appendix A) and selective $^1O_2$ generation synergistically contributed to the excellent degradation performance of the Co–O–Fe dual-site/O_3 system, resulting in a 4.0-fold increase in the ozone utilization index (Fig. S26 in Appendix A) [10,11,57].

To evaluate the versatility of the Co–O–Fe dual-site/O_3 system in degrading various organic pollutants with high IPs, we screened six representative compounds: 4-AP, HQ, phenol, 4-CP, 4-NP, and 4-NC. The chemical structures and corresponding IP values of these pollutants are presented in Fig. 4(a). The degradation performances and k_{obs} for the six pollutants were carefully assessed, demonstrating the selectivity of the Co–O–Fe dual-site/O_3 system when

targeting organic compounds with various IP values (Fig. S27 in Appendix A). Specifically, the Co–O–Fe dual-site/O_3 system achieved a degradation rate exceeding 96% for 4-CP, phenol, HQ, and 4-AP within 10 min. These compounds possess electron-donating groups (EDG) that increase the electron density of the benzene ring, facilitating their oxidation (Fig. S27(a)). Conversely, pollutants containing electron-withdrawing groups (EWG) (such as $-NO_2$ and –Cl) exhibited slightly lower degradation rates, with 85% removal for 4-NP and 77% for 4-NC in the Co–O–Fe dual-site/O_3 system. Fig. S27(b) shows the fitting results of the degradation rates through pseudo-first-order kinetics for the screened organics, with the k_{obs} values summarized in Fig. 4(b). Among these, 4-AP, which contains a strong EDG ($-NH_2$), displayed the highest k_{obs} value of 0.51 min^{-1}, whereas 4-NP, with a strong EWG ($-NO_2$), had a k_{obs} value of 0.20 min^{-1}. Notably, 4-CN, which possesses two EWG ($-NO_2$ and –Cl), exhibited the lowest k_{obs} value of 0.15 min^{-1}. These results underscore the selective efficacy of the Co–O–Fe dual-site/O_3 system against electron-rich pollutants, driven by the mild oxidation potential of $^1O_2$ [62,63]. On the basis of these findings, we hypothesize that the electron-donating or electron-withdrawing abilities of substituent groups significantly influence the oxidation reactions with $^1O_2$ and thus impact the system's degradation performance [19,62,63]. In the degradation process dominated by $^1O_2$, electron-rich pollutants with functional groups such as $-NH_2$, –OH, and -R are expected to act as electron donors, making them prone to electrophilic attack by $^1O_2$. To validate this assumption, we used the IP of organic pollutants as an indicator of their electron-donating or electron-withdrawing capacity. As illustrated in Fig. 4(b), a strong negative linear correlation was observed between the IP values and the k_{obs} values of the organic pollutants, suggesting that organic compounds with higher electron-withdrawing capacities (i.e., higher IP values) tend to compromise the degradation efficiency of the Co–O–Fe dual-site/O_3 system. The performance of the Co–O–Fe dual-site also

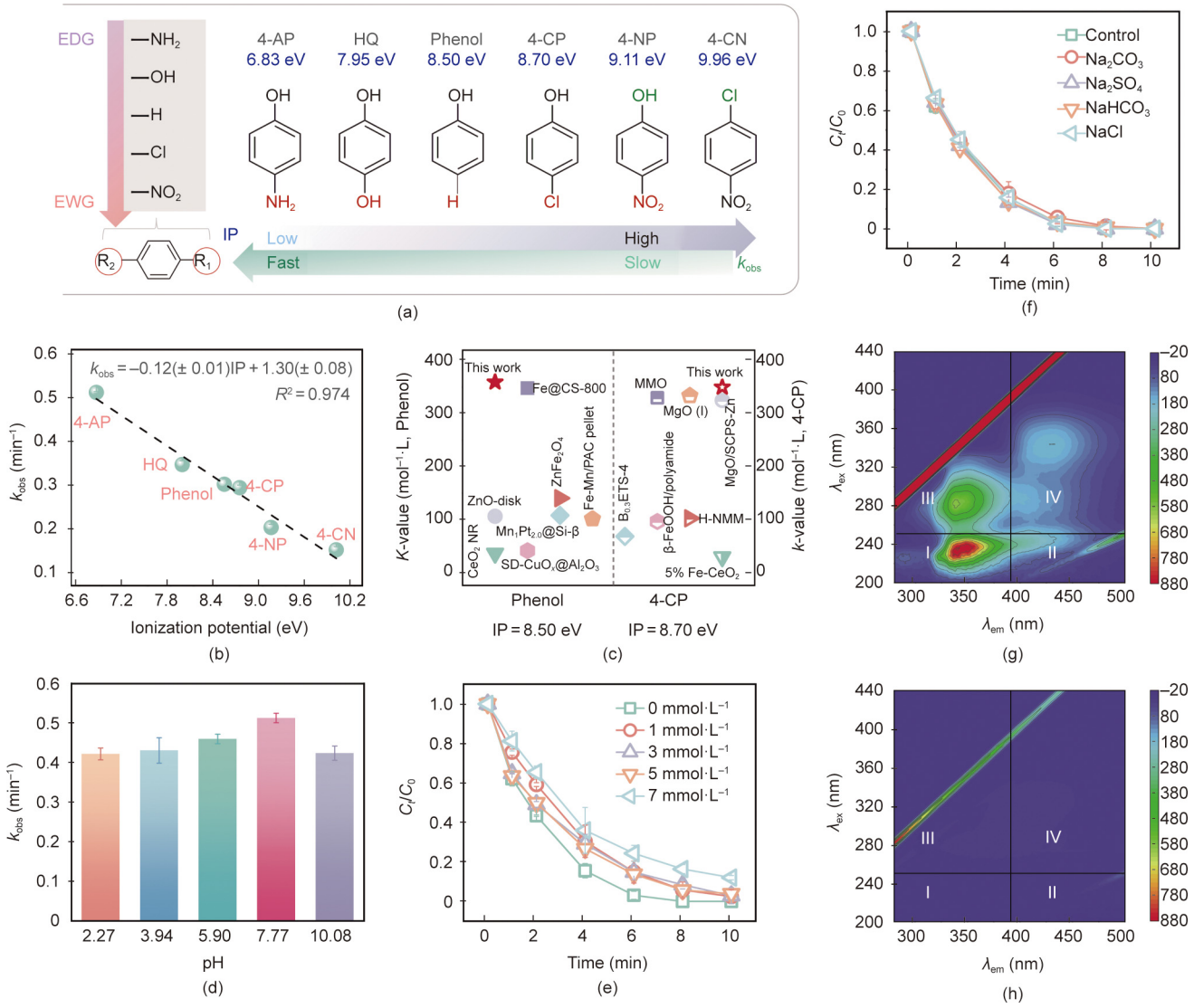

Fig. 4. Catalytic ozonation performance of the asymmetric Co–O–Fe dual-sites. (a) Organic pollutants with various IPs and their chemical structures. (b) The correlation between the k_{obs} and IP values. (c) Comparison of phenol and 4-CP degradation performance with that of recently reported catalytic ozonation processes. The modified kinetic rate constant (*K*-value) was calculated through dividing the k_{obs} of contaminants by catalyst dosage and ozone concentration, followed by multiplying contaminant concentration. Influences of (d) initial pH, (e) HA, and (f) salts on phenol degradation in the Co–O–Fe/O_3 system. Three-dimensional excitation-emission matrix (3D-EEM) spectra of collected primary effluents (g) before and (h) after treatment with the Co–O–Fe/O_3 system for 30 min. λ_{ex} and λ_{em} indicate the excitation wavelength and emission wavelength, respectively. Reaction conditions: ozone input dosage = 0.42 $mmol \cdot L^{-1} \cdot min^{-1}$, catalysts = 0.1 $g \cdot L^{-1}$, $C_{pollutants,\ 0}$ for (b) = 50 $mg \cdot L^{-1}$, $C_{phenol,\ 0}$ for (d–f) = 20 $mg \cdot L^{-1}$, $C_{salts,\ 0}$ = 200 $mg \cdot L^{-1}$, T = 25 °C.

outperforms that of many state-of-the-art catalysts, demonstrating superior activity for pollutant degradation (Fig. 4(c), Table S8 in Appendix A). In summary, disrupting the symmetry of the iron sites via cobalt doping alters the ozone activation pathway and facilitates the selective and effective generation of $^1O_2$, significantly contributing to the degradation of a variety of organic pollutants with high IPs.

3.5. Practical considerations of asymmetric Co–O–Fe dual-sites for efficient wastewater treatments

Before evaluating the practicality of the asymmetric Co–O–Fe dual-site/O_3 system, we systematically investigated the impacts of pH, interfering ions, and dissolved organic matter on degradation performance. The asymmetric Co–O–Fe dual-site demonstrates significant pH resistance, operating effectively within a range from 2.27–7.77. Although there was a slight decrease in the k_{obs} at an initial pH of 10.08 due to surface repulsion and hydroxide ion (OH^-) quenching effects on $^1O_2$ (Fig. 4(d), Fig. S28 in Appendix A) [19], the overall performance remained robust. Furthermore, the phenol degradation efficiency of the established HCO system is highly resistant to the inhibitory effects of various salts (e.g., Na_2SO_4, $NaHCO_3$, Na_2CO_3, and NaCl) and HA at all tested concentrations (Figs. 4(e) and (f), Fig. S29 in Appendix A), emphasizing its robustness in complex water matrices. After eight consecutive cycles, the asymmetric Co O Fe dual site exhibited negligible loss in catalytic activity for phenol degradation, maintaining a removal rate close to 100% and a k_{obs} value of approximately 0.52 min^{-1} (Fig. S30 in Appendix A). The PXRD pattern of MIL-53(FeCo) after repeated use (Fig. S31 in Appendix A) shows increased intensities of the characteristic peaks at 12.6° and 17.6°, which can be attributed to the increased formation of irregular flakes. The FT–IR spectrum (Fig. S32 in Appendix A) of the MIL-53(FeCo) remained almost identical to that of the pristine catalyst, indicating outstanding stability and reusability under the reaction conditions.

Furthermore, we assessed the practical application of the system in real-world scenarios. Specifically, we evaluated its effectiveness in treating refractory textile industrial wastewater, which is characterized by high phenol content and salinity, posing significant purification challenges. Using three-dimensional excitation-emission matrix (3D-EEM) fluorescence spectroscopy (Figs. 4(g)–(h)), we demonstrated the complete removal of aromatic proteins, soluble microbial byproduct analogs, and humic acid-like organics from both primary and secondary textile effluents, even at high specific conductance levels (Figs. S33 and S34 in Appendix A), after just 30 min of treatment with the asymmetric Co–O–Fe dual-site/O_3 system. Additionally, the system achieved a nearly 50% reduction in chemical oxygen demand (COD) in the secondary textile effluent (Table S9 in Appendix A), demonstrating substantial COD removal efficiency. Furthermore, the pH and COD levels of the secondary textile effluent after treatment comply with the standards set by FZ/T 01107-2011 for water reuse in textile dyeing and finishing, issued by the Ministry of Industry and Information Technology of China. Given the inherent challenges associated with treating textile industrial wastewaters, the practical performance of the asymmetric Co–O–Fe dual-site is potent. Moreover, secondary effluents from the surfactant, chemical, and medical industries were collected to further assess the practicability of the asymmetric Co–O–Fe dual-site/O_3 system. The results from 3D-EEM fluorescence spectroscopy (Fig. S35 in Appendix A) and COD measurements (Table S10 in Appendix A) confirmed that the system maintained excellent performance in treating diverse types of industrial wastewater. Overall, the asymmetric Co–O–Fe dual-site/O_3 system shows exceptional adaptability, durability, and decontamination efficacy in addressing complex wastewaters, underscoring its significant feasibility for practical water purification applications.

4. Conclusions

In this study, we successfully developed an asymmetric Co–O–Fe dual-site configuration by disrupting the Fe–O–Fe symmetry in monometallic MIL-53(Fe) through cobalt incorporation. This innovation addresses the limitations of ozone activation and enhances selective $^1O_2$ generation for the sustainable degradation of pollutants with high-IPs. Our experimental and theoretical analyses collectively demonstrate that the optimized electron arrangement in the asymmetric Co–O–Fe dual-sites contributes to a significant improvement in $^1O_2$ selectivity by promoting ozone adsorption, thereby reducing the energy barrier for O–O bond scission. We observed a 2.4-fold increase in the nonradical pathway for ozone activation, reflected by the steady-state concentration of $^1O_2$, whereas the radical pathway exhibited a 1.9-fold reduction in terms of accumulated ·OH generation. Compared with the symmetric Fe–O–Fe configuration, the established asymmetric Co–O–Fe dual-site achieved remarkable increases in $^1O_2$ selectivity (6.6-fold) and phenol degradation efficiency (2.0-fold), significantly surpassing the existing benchmarks and state-of-the-art ozonation catalyst counterparts. Eventually, the Co–O–Fe dual-site/O_3 system enables the efficient and sustainable removal of various high-impact organic pollutants from complex water matrices. The observed positive linear correlation between the k_{obs} and theoretical IP values indicates the unique and robust contribution of $^1O_2$ to wastewater treatment with high feasibility and practicality. This work represents a significant advancement in the development of next-generation ozonation catalysts with substantial practical potential for sustainable water purification and beyond.

CRediT authorship contribution statement

Qian Hu: Writing – original draft, Visualization, Validation, Methodology, Conceptualization. **Shanli Wang:** Writing – review & editing, Investigation. **Kaixing Fu:** Visualization, Data curation. **Guangpeng Yang:** Software, Data curation. **Licong Xu:** Validation, Formal analysis. **Wenbin Jiang:** Validation, Investigation. **Minghua Wu:** Project administration. **Wangyang Lu:** Resources. **Xiaomin Zhu:** Supervision. **Jinming Luo:** Supervision, Funding acquisition, Conceptualization.

Declaration of competing interest

The authors declare that they have no known competing financial interests or personal relationships that could have appeared to influence the work reported in this paper.

Acknowledgments

This work was supported by the National Natural Science Foundation of China (22176124), the Zhejiang Provincial Postdoctoral Science Foundation (ZJ2024003), and the Research Start-up Funding from Shanghai Jiao Tong University (WH220416002). The views and ideas expressed herein are solely those of the authors and do not represent the ideas of the funding agencies in any form.

Compliance with ethics guidelines

Qian Hu, Shanli Wang, Kaixing Fu, Guangpeng Yang, Licong Xu, Wenbin Jiang, Minghua Wu, Wangyang Lu, Xiaomin Zhu, and Jinming Luo declare that they have no conflicts of interest or financial conflicts to disclose.

Appendix A. Supplementary data

Supplementary data to this article can be found online at https://doi.org/10.1016/j.eng.2025.12.016.

References

[1] Mekonnen MM, Hoekstra AY. Four billion people facing severe water scarcity. Sci Adv 2016;2(2):e1500323.
[2] Eliasson J. The rising pressure of global water shortages. Nature 2015;517:6.
[3] Chen Z, An F, Zhang Y, Liang Z, Liu W, Xing M. Single-atom Mo–Co catalyst with low biotoxicity for sustainable degradation of high-ionization-potential organic pollutants. Proc Natl Acad Sci USA 2023;120(29):e2305933120.
[4] Zhang J, Shan C, Zhang W, Pan B. *In situ* ligand-modulated activation of inert Ce (III/IV) into ozonation catalyst for efficient water treatment. Proc Natl Acad Sci USA 2023;120(35):e2305255120.
[5] Guo Y, Long J, Huang J, Yu G, Wang Y. Can the commonly used quenching method really evaluate the role of reactive oxygen species in pollutant abatement during catalytic ozonation? Water Res 2022;215:118275.
[6] Wang Y, Duan X, Xie Y, Sun H, Wang S. Nanocarbon-based catalytic ozonation for aqueous oxidation: engineering defects for active sites and tunable reaction pathways. ACS Catal 2020;10(22):13383–414.
[7] Zhou Q, Song C, Wang P, Zhao Z, Li Y, Zhan S. Generating dual-active species by triple-atom sites through peroxymonosulfate activation for treating micropollutants in complex water. Proc Natl Acad Sci USA 2023;120(13):e2300085120.
[8] Wu Z, Huang B, Wang X, He CS, Liu Y, Du Y, et al. Facilely tuning the first-shell coordination microenvironment in iron single-atom for Fenton-like chemistry toward highly efficient wastewater purification. Environ Sci Technol 2023;57(37):14046–57.
[9] Ren T, Yin M, Chen S, Ouyang C, Huang X, Zhang X. Single-atom Fe-N_4 sites for catalytic ozonation to selectively induce a nonradical pathway toward wastewater purification. Environ Sci Technol 2023;57(9):3623–33.
[10] Yu G, Wang Y, Cao H, Zhao H, Xie Y. Reactive oxygen species and catalytic active sites in heterogeneous catalytic ozonation for water purification. Environ Sci Technol 2020;54(10):5931–46.
[11] Hu Q, Zhang M, Xu L, Wang S, Yang T, Wu M, et al. Unraveling timescale-dependent Fe-MOFs crystal evolution for catalytic ozonation reactivity modulation. J Hazard Mater 2022;431:128575.
[12] Wei K, Cao X, Gu W, Liang P, Huang X, Zhang X. Ni-induced C-Al_2O_3-framework ($_{Ni}$CAF) supported core-multishell catalysts for efficient catalytic ozonation: a structure-to-performance study. Environ Sci Technol 2019;53(12):6917–26.
[13] Wang Y, Chen L, Cao H, Chi Z, Chen C, Duan X, et al. Role of oxygen vacancies and Mn sites in hierarchical Mn_2O_3/$LaMnO_{3-\delta}$ perovskite composites for aqueous organic pollutants decontamination. Appl Catal B 2019;245:546–54.
[14] Li X, Liu L, Ren X, Gao J, Huang Y, Liu B. Microenvironment modulation of single-atom catalysts and their roles in electrochemical energy conversion. Sci Adv 2020;6(39):eabb6833.
[15] Xiao M, Chen Y, Zhu J, Zhang H, Zhao X, Gao L, et al. Climbing the apex of the ORR volcano plot via binuclear site construction: electronic and geometric engineering. J Am Chem Soc 2019;141(44):17763–70.
[16] Zhou W, Su H, Cheng W, Li Y, Jiang J, Liu M, et al. Regulating the scaling relationship for high catalytic kinetics and selectivity of the oxygen reduction reaction. Nat Commun 2022;13(1):6414.
[17] Wang Z, Yi Z, Wong LW, Tang X, Wang H, Wang H, et al. Oxygen doping cooperated with Co–N–Fe dual-catalytic sites: synergistic mechanism for catalytic water purification within nanoconfined membrane. Adv Mater 2024;36(30):2404278.
[18] Zhao Z, Wang P, Song C, Zhang T, Zhan S, Li Y. Enhanced interfacial electron transfer by asymmetric Cu-O_v-in sites on In_2O_3 for efficient peroxymonosulfate activation. Angew Chem Int Ed 2023;62(11):e202216403.
[19] Gu CH, Wang S, Zhang AY, Liu C, Jiang J, Yu HQ. Tuning electronic structure of metal-free dual-site catalyst enables exclusive singlet oxygen production and in-situ utilization. Nat Commun 2024;15(1):5771.
[20] Song J, Hou N, Liu X, Antonietti M, Zhang P, Ding R, et al. Asymmetrically coordinated CoB_1N_3 moieties for selective generation of high-valence Co-oxo species via coupled electron–proton transfer in Fenton-like reactions. Adv Mater 2023;35(23):2209552.
[21] Yao Y, Wang C, Yang Y, Zhang S, Yan X, Xiao C, et al. Mn–Co dual sites relay activation of peroxymonosulfate for accelerated decontamination. Appl Catal B 2023;330:122656.
[22] Cai G, Yan P, Zhang L, Zhou HC, Jiang HL. Metal–organic framework-based hierarchically porous materials: synthesis and applications. Chem Rev 2021;121(20):12278–326.
[23] Islamoglu T, Chen Z, Wasson MC, Buru CT, Kirlikovali KO, Afrin U, et al. Metal–organic frameworks against toxic chemicals. Chem Rev 2020;120(16):8130–60.
[24] Sanati S, Morsali A, García H. First-row transition metal-based materials derived from bimetallic metal–organic frameworks as highly efficient electrocatalysts for electrochemical water splitting. Energy Environ Sci 2022;15(8):3119–51.
[25] Liu L, Corma A. Bimetallic sites for catalysis: from binuclear metal sites to bimetallic nanoclusters and nanoparticles. Chem Rev 2023;123(8):4855–933.
[26] Yu D, Wang L, Yang T, Yang G, Wang D, Ni H, et al. Tuning Lewis acidity of iron-based metal–organic frameworks for enhanced catalytic ozonation. Chem Eng J 2021;404:127075.
[27] Yu D, Wu M, Hu Q, Wang L, Lv C, Zhang L. Iron-based metal–organic frameworks as novel platforms for catalytic ozonation of organic pollutant: efficiency and mechanism. J Hazard Mater 2019;367:456–64.
[28] Luo YR. Comprehensive handbook of chemical bond energies. Boca Raton, FL: CRC Press; 2007.
[29] Horcajada P, Serre C, Maurin G, Ramsahye NA, Balas F, Vallet-Regí M, et al. Flexible porous metal–organic frameworks for a controlled drug delivery. J Am Chem Soc 2008;130(21):6774–80.
[30] Hou J, Ashling CW, Collins SM, Krajnc A, Zhou C, Longley L, et al. Metal–organic framework crystal-glass composites. Nat Commun 2019;10(1):2580.
[31] Zhu Y, Ren B, Qiu Y, Zhou Q, Chang J, Lin Z, et al. Nanoporous cerium-doped MIL-53(Fe)-NH_2 for effective and selective removal of phosphate from wastewater. ACS Appl Nano Mater 2024;7(17):20700–13.
[32] Wu Q, Siddique MS, Guo Y, Wu M, Yang Y, Yang H. Low-crystalline bimetallic metal–organic frameworks as an excellent platform for photo-Fenton degradation of organic contaminants: intensified synergism between hetero-metal nodes. Appl Catal B 2021;286:119950.
[33] Yang T, Yu D, Wang D, Yang T, Li Z, Wu M, et al. Accelerating Fe(III)/Fe(II) cycle via Fe(II) substitution for enhancing Fenton-like performance of Fe-MOFs. Appl Catal B 2021;286:119859.
[34] Roy D, Neogi S, De S. Visible light assisted activation of peroxymonosulfate by bimetallic MOF based heterojunction MIL-53(Fe/Co)/CeO_2 for atrazine degradation: pivotal roles of dual redox cycle for reactive species generation. Chem Eng J 2022;430:133069.
[35] Liu Y, Wang C, Ju S, Li M, Yuan A, Zhu G. FeCo-based hybrid MOF derived active species for effective oxygen evolution. Prog Nat Sci Mater Intern 2020;30(2):185–91.
[36] Breeze MI, Clet G, Campo BC, Vimont A, Daturi M, Grenèche JM, et al. Isomorphous substitution in a flexible metal–organic framework: mixed-metal, mixed-valent MIL-53(Fe) type materials. Inorg Chem 2013;52(14):8171–82.
[37] Liu K, Wang X, Wang N, Zhang R, Yang M, Hou B, et al. Effective electrochemical water oxidation to H_2O_2 based on a bimetallic Fe/Co metal–organic framework. Energy Adv 2024;3(11):2842–50.
[38] Abuzalat O, Tantawy H, Mokhtar M, Baraka A. Nano-porous bimetallic organic frameworks (Fe/Co)-BDC, a breathing MOF for rapid and capacitive removal of Cr-oxyanions from water. J Water Process Eng 2022;46:102537.
[39] Sunil J, Narayana C, Kumari G, Jayaramulu K. Raman spectroscopy, an ideal tool for studying the physical properties and applications of metal–organic frameworks (MOFs). Chem Soc Rev 2023;52(10):3397–437.
[40] Shen P, Hou K, Chen F, Pi Z, He L, Chen S, et al. Ultra-rapid and long-lasting activation of peracetic acid by Cu–Co spinel oxides for eliminating organic contamination: role of radical and non-radical catalytic oxidation. Chem Eng J 2023;463:142344.
[41] Wang Q, Lu J, Jiang Y, Yang S, Yang Y, Wang Z. FeCo bimetallic metal organic framework nanosheets as peroxymonosulfate activator for selective oxidation of organic pollutants. Chem Eng J 2022;443:136483.
[42] Zheng Y, Liu Q, Shan C, Su Y, Fu K, Lu S, et al. Defective ultrafine MnO_x nanoparticles confined within a carbon matrix for low-temperature oxidation of volatile organic compounds. Environ Sci Technol 2021;55(8):5403–11.
[43] Deng L, Hung SF, Liu S, Zhao S, Lin ZY, Zhang C, et al. Accelerated proton transfer in asymmetric active units for sustainable acidic oxygen evolution reaction. J Am Chem Soc 2024;146(33):23146–57.
[44] Ha M, Kim DY, Umer M, Gladkikh V, Myung CW, Kim KS. Tuning metal single atoms embedded in N_xC_y moieties toward high-performance electrocatalysis. Energy Environ Sci 2021;14(6):3455–68.
[45] Zhang XY, Li FT, Dong YW, Dong B, Dai FN, Liu CG, et al. Dynamic anion regulation to construct S-doped FeOOH realizing 1000 mA cm^{-2}-level-current-density oxygen evolution over 1000 h. Appl Catal B 2022;315:121571.
[46] Zhang C, Qi Q, Mei Y, Hu J, Sun M, Zhang Y, et al. Rationally reconstructed metal–organic frameworks as robust oxygen evolution electrocatalysts. Adv Mater 2023;35(8):2208904.
[47] Zhang B, Shen Y, Liu B, Ji J, Dai W, Huang P, et al. Boosting ozone catalytic oxidation of toluene at room temperature by using hydroxyl-mediated MnO_x/Al_2O_3 catalysts. Environ Sci Technol 2023;57(17):7041–50.
[48] Huang M, Li YS, Zhang CQ, Cui C, Huang QQ, Li M, et al. Facilely tuning the intrinsic catalytic sites of the spinel oxide for peroxymonosulfate activation: from fundamental investigation to pilot-scale demonstration. Proc Natl Acad Sci USA 2022;119(30):e2202682119.
[49] Zhao Z, Tan H, Zhang P, Liang X, Li T, Gao Y, et al. Turning the inert element zinc into an active single-atom catalyst for efficient Fenton-like chemistry. Angew Chem Int Ed 2023;62(18):e202219178.
[50] Foley S, Rotureau P, Pin S, Baldacchino G, Renault JP, Mialocq JC. Radiolysis of confined water: production and reactivity of hydroxyl radicals. Angew Chem Int Ed 2005;44(1):110–2.
[51] Gao Y, Chen Z, Zhu Y, Li T, Hu C. New insights into the generation of singlet oxygen in the metal-free peroxymonosulfate activation process: important role of electron-deficient carbon atoms. Environ Sci Technol 2020;54(2):1232–41.
[52] Guo Y, Zhang Y, Yu G, Wang Y. Revisiting the role of reactive oxygen species for pollutant abatement during catalytic ozonation: the probe approach versus the scavenger approach. Appl Catal B 2021;280:119418.

[53] Guo Y, Zhan J, Yu G, Wang Y. Evaluation of the concentration and contribution of superoxide radical for micropollutant abatement during ozonation. Water Res 2021;194:116927.
[54] Zhou Y, Zhou Q, Liu H, Xu W, Wang Z, Qiao S, et al. Asymmetric dinitrogen-coordinated nickel single-atomic sites for efficient CO_2 electroreduction. Nat Commun 2023;14(1):3776.
[55] Zeng Y, Zhao J, Wang S, Ren X, Tan Y, Lu YR, et al. Unraveling the electronic structure and dynamics of the atomically dispersed iron sites in electrochemical CO_2 reduction. J Am Chem Soc 2023;145(28):15600–10.
[56] Qu W, Luo M, Tang Z, Zhong T, Zhao H, Hu L, et al. Accelerated catalytic ozonation in a mesoporous carbon-supported atomic Fe-N_4 sites nanoreactor: confinement effect and resistance to poisoning. Environ Sci Technol 2023;57(35):13205–16.
[57] Qu W, Tang Z, Tang S, Zhong T, Zhao H, Tian S, et al. Precisely constructing orbital coupling-modulated iron dinuclear site for enhanced catalytic ozonation performance. Proc Natl Acad Sci USA 2024;121(16):e2319119121.
[58] Ma D, Lian Q, Zhang Y, Huang Y, Guan X, Liang Q, et al. Catalytic ozonation mechanism over M_1-N_3C_1 active sites. Nat Commun 2023;14(1):7011.
[59] Yu G, Wu Y, Cao H, Ge Q, Dai Q, Sun S, et al. Insights into the mechanism of ozone activation and singlet oxygen generation on N-doped defective nanocarbons: a DFT and machine learning study. Environ Sci Technol 2022;56(12):7853–63.
[60] Liang L, Cao J, Zhang Y, Liu X, Li J, Yang B, et al. Selective adsorption of high ionization potential value organic pollutants in wastewater. Proc Natl Acad Sci USA 2024;121(29):e2403766121.
[61] Thommes M, Kaneko K, Neimark AV, Olivier JP, Rodriguez-Reinoso F, Rouquerol J, et al. Physisorption of gases, with special reference to the evaluation of surface area and pore size distribution (IUPAC technical report). Pure Appl Chem 2015;87(9–10):1051–69.
[62] Hu P, Su H, Chen Z, Yu C, Li Q, Zhou B, et al. Selective degradation of organic pollutants using an efficient metal-free catalyst derived from carbonized polypyrrole via peroxymonosulfate activation. Environ Sci Technol 2017;51(19):11288–96.
[63] Liu X, Qin H, Xing S, Liu Y, Chu C, Yang D, et al. Selective removal of organic pollutants in groundwater and surface water by persulfate-assisted advanced oxidation: the role of electron-donating capacity. Environ Sci Technol 2023;57(36):13710–20.